Depoling phenomena in $Na_{0.5}Bi_{0.5}TiO_3$-$BaTiO_3$: A structural perspective

Gobinda Das Adhikary,[1] Bhoopesh Mahale,[1] Badari Narayana Rao,[1,*] Anatoliy Senyshyn,[2] and Rajeev Ranjan[1,†]

[1]*Department of Materials Engineering, Indian Institute of Science, Bangalore-560012, India*

[2]*Forschungsneutronenquelle Heinz Maier-Leibnitz (FRM II). Technische Universität München, Lichtenbergestrasse 1, D-85747 Garching b. München, Germany*

(Received 5 March 2020; revised 22 March 2021; accepted 28 April 2021; published 12 May 2021)

The structural complexities of the lead-free piezoelectric system $(1\text{-}x)Na_{0.5}Bi_{0.5}TiO_3$-$xBaTiO_3$ (NBT-BT) continues to pose challenge regarding understanding the mechanisms underlying several interesting phenomena. Issues like (i) whether thermal depoling across compositions is triggered by a structural transformation event or not, (ii) what causes the average *Cc* structure to partially transform to *R*3*c* at $x \sim 0.03$ in unpoled specimens, (iii) what makes complete depoling of the compositions $0.03 \leqslant x \leqslant 0.05$ occur in a considerably small temperature interval as compared to those for $x < 0.03$, (iv) what makes the *R*3*c*-*P*4*bm* transition temperature (T_2) abruptly become smaller than the depolarization temperature (T_d) at $x = 0.06$, etc., have remain unresolved. Here, we offer structural insights on these issues by carrying out a detailed investigation using a set of complementary tools involving temperature-dependent x-ray powder diffraction, neutron powder diffraction, dielectric, ferroelectric, piezoelectric, and thermally induced depoling current measurements. We show that onset of thermal depoling in NBT ($x = 0$) well below its depolarization temperature is caused by abrupt reduction of intrinsic polarization in the ferroelectric *R*3*c* phase, triggered by the appearance of the *P*4*bm* phase. Our study suggests that partial conversion of the *Cc* average structure to *R*3*c* in unpoled NBT-BT at $x \sim 0.03$ (more precisely in the range $0.03 \leqslant x \leqslant 0.05$) is catalyzed by the appearance of *P*4*bm* phase. The overlap of T_d and T_2 for this composition range is correlated with the collapse of the tetragonality of the *P*4*bm* phase and significantly reduced kinetic barrier associated with the *R*3*c* $\rightarrow$ *P*4*bm* transformation. We show that the abrupt crossover between T_d and T_2 at $x = 0.06$ is due to takeover of the thermal depoling process by an emergent tetragonal (*P*4*mm*)-like ferroelectric distortion. We present updated phase diagrams of poled and unpoled specimens which highlight all the subtle details needed to explain the temperature-dependent properties of this complex piezoelectric alloy system.

DOI: 10.1103/PhysRevB.103.184106

I. INTRODUCTION

Oxide perovskite-based piezoelectrics are extensively used in wide-ranging applications as actuator, ultrasonic motors, and sensors. While for over five decades $Pb(Zr_xTi_{1-x})O_3$ (PZT)-based piezoelectrics have been the most preferred choice [1], new legislations/regulations in the past two decades have compelled the scientific and technological community to seek lead-free alternatives [2]. The subsequent surge of interest has led to development of Pb-free piezoelectric materials with large electromechanical properties in $BaTiO_3$ [3–12], $K_{0.5}Na_{0.5}NbO_3$ (KNN) [13–16], and $Na_{0.5}Bi_{0.5}TiO_3$ (NBT) [17–24]-based ferroelectric solid solutions. Although very large piezoelectric coefficients ($d_{33} \sim 600$ pC/N) have been reported in $BaTiO_3$-based compositions, they have the drawback of low Curie-point (~80 °C). Similarly, despite the large $d_{33} \sim 500$ pC/N reported in complex multielement doped KNN compositions [15], the strong dependence of properties on synthesis conditions poses problems in reproducibility of the properties. NBT-based piezoelectrics are among the preferable choices because, despite their comparatively low piezoelectric properties ($d_{33} \sim 200$ pC/N), the ease of reproducibility of properties and moderately high Curie point are important advantages. The comparatively lower density makes NBT-based piezoelectrics promising Pb-free alternative in high-power applications [25]. Some derivatives of NBT at the ergodic-nonergodic threshold exhibit very large electrostrain (~0.7%) [26,27].

An important consideration for piezoelectric materials for use in high-power devices is stability of their electromechanical properties against unintentional increase in temperature during the operation of the device, as depoling of the piezoelectric element can render the device nonfunctional. For normal ferroelectric-based piezoelectrics such as PZT and $Ba(Ti, Zr)O_3$ [28], the depolarization temperature is the Curie point. $Na_{0.5}Bi_{0.5}TiO_3$, on the other hand, belongs to the category of relaxor ferroelectrics [29–32], the thermal depoling of which is generally benchmarked against the depolarization temperature (T_d) of the system. Although thermal depoling may occur over a range of temperature, most studies in the past have focused attention on the depolarization temperature (T_d) at which (i) the relative permittivity increases abruptly, (ii) piezoelectric response decreases dramatically, and (iii) thermally induced depoling current shows a peak on heating of poled specimens.

*Current address: Center for Frontier Science, Chiba University, 1-33 Yayoi-cho, Inage-ku, Chiba-shi, Chiba, 263-8522 Japan.

†rajeev@iisc.ac.in

The end member NBT exhibits two structural transformations: rhombohedral ($R3c$)-tetragonal ($P4bm$) at ∼255 °C and tetragonal ($P4bm$)-cubic ($Pm\bar{3}m$) at 540 °C [33]. The $P4bm$ phase is characterized by in-phase ($a^0a^0c^+$) octahedral tilt, the residue of which survives at room temperature on a mesoscopic scale [34,35]. The consequent positional disorder, which also involves nonrhombohedral displacement of the Na/Bi cations [36–38], imparts relaxor ferroelectric character to the system. It is also responsible for making the average structure of unpoled NBT appear as monoclinic (Cc) [39–41], instead of rhombohedral ($R3c$) reported earlier [42]. Poling, however, irreversibly transforms the average Cc structure to $R3c$ by suppressing the structural disorder [41,43]. Dorcet *et al.* [44] argued that depolarization of NBT at $T_d \sim 200$ °C is associated with the intergrowth of orthorhombic ($Pnma$) domains within the ferroelectric rhombohedral ($R3c$) matrix. X-ray diffraction [32], Raman studies [45], and elastic property measurement [46], however, do not corroborate this conclusion. Aksel *et al.* [45,47] pointed out that thermal depoling of NBT occurs over a noticeably large temperature range 140–200 °C. Based on structural analysis [using x-ray diffraction (XRD)] of unpoled specimens the authors concluded that thermal depoling is not associated with any distinct structural event [45,47]. Rao *et al.* [48] correlated the onset of depoling at ∼150 °C with the onset of the in-phase tilt. However, the work did not explain how this influences the structural features of the ferroelectric rhombohedral ($R3c$) phase which sustains the long-range ferroelectric order. Ambiguity also persists regarding the thermal depoling mechanisms for the two important solid solutions of NBT, namely $(1\text{-}x)Na_{0.5}Bi_{0.5}TiO_3$-$xBaTiO_3$ (NBT-BT) [16,20,29,49–51] and $(1\text{-}y)Na_{0.5}Bi_{0.5}TiO_3$-$yK_{0.5}Bi_{0.5}TiO_3$(NBT-KBT) [17,18,21,24,52]. Both the systems exhibit morphotropic phase boundary (MPB) at $x = 0.06$ and $y = 0.20$, respectively.

In the present work we have focused our attention on NBT-BT. Except for the difference in the compositional and temperature ranges, the broader aspects of the depoling mechanisms presented here are expected to be relevant for the NBT-KBT system also. X-ray-diffraction studies of unpoled NBT-BT at room temperature suggest that NBT-BT exhibits Cc average structure for $x < 0.03$ [22,39,40,48], $R3c$ for $0.03 \leqslant x \leqslant 0.05$, and "cubiclike" for $0.06 \leqslant x \leqslant 0.07$ [49]. Ma *et al.* reported that unpoled NBT-BT exhibits a Cc-$R3c$ boundary at $x \sim 0.03$; both phases coexist in a narrow composition interval $0.02 < x < 0.05$ [22]. The $P4bm$ (relaxor) phase has been reported in a wide composition interval ($0.05 < x \leqslant 0.11$) at room temperature [22]. In contrast, all poled NBT-BT exhibit $R3c$ average structure for $x \leqslant 0.06$ [53,54], tetragonal (with $P4mm$-like ferroelectric distortion) for $x \geqslant 0.07$ [55]. Poled $x = 0.065$ exhibits coexistence of rhombohedral ($R3c$) and tetragonal ($P4mm$) distortions [56]. Given that for $x \leqslant 0.07$, the average structure of poled specimens appears remarkably different from their unpoled counterparts, attempts at establishing a structural correspondence, if any, with thermal depoling behavior of the different compositions of this series requires temperature-dependent structural analysis of poled specimens during the heating cycle.

A summary of how thermal depolarization temperature (T_d) compares with the $R3c$-$P4bm$ transition temperature (labeled as T_2 in Ref. [46]) for different compositions of NBT-BT has been reported in the phase diagram of Cordero *et al.* [46]. The following features of this diagram are worth noting: (i) T_d is significantly less than T_2 for $x < 0.03$, (ii) both temperatures almost overlap in the composition interval $0.03 \leqslant x \leqslant 0.05$, and (iii) $T_d > T_2$ at $x = 0.06$. It is interesting to note that the composition ($x \sim 0.03$) at which T_d and T_2 almost overlap [46] coincides with composition for which Ma *et al.* reported the Cc-$R3c$ boundary [22]. There is no clarity if the two seemingly independent phenomena ($Cc/R3c$ phase boundary, and the overlap of T_2 and T_d) at $x \sim 0.03$ have a common origin or is a mere coincidence. Given that the Cc structure of unpoled NBT is a special manifestation on the global scale of the assemblages of nanosized in-phase tilted regions coherently embedded in the regions comprising $a^-a^-a^-$ antiphase tilt, resulting in an average $a^-a^-c^-$ tilt system [57], the $Cc/R3c$ boundary most likely suggests breaking of these coherent assemblages. The factor which disrupts this coherent assemblage is still not known. The abrupt crossover between T_2 and T_d at $x = 0.06$ shown in the phase diagram of Cordero *et al.* [46] is another puzzle which remain unexplained so far. In a related observation Jo *et al.* [58,59] argued that poled $x = 0.06$ transforms to a relaxor state in a two-step process—the domains first lose their ferroelectric-ferroelastic texture and subsequently dissociate into nanoscale entities. The mechanism which causes detexturing in the first place has not been settled. In the present work we have investigated these important issues using temperature-dependent neutron powder diffraction, x-ray powder diffraction, dielectric, piezoelectric, and depoling current measurements. While the better resolution of the x-ray-diffraction data allowed us to identify the nature of weak lattice distortions, neutron powder-diffraction data offered valuable insights on the nature of octahedral tilt (the signature superlattice peaks of which are not visible in the XRD patterns). The results have been used to present an updated composition-temperature phase diagram of NBT-BT.

II. EXPERIMENT

$(1\text{-}x)Na_{0.5}Bi_{0.5}TiO_3$-$(x)BaTiO_3$ (NBT-xBT) specimens ($0.00 \leqslant x \leqslant 0.20$) were prepared using the conventional solid-state route. Dried powders of Na_2CO_3 (99.9%, Sisco Research Laboratories Pvt. Ltd. [SRL]), $BaCO_3$ (99%, SRL), Bi_2O_3 (99%, SRL), TiO_2 (99.8%, Alfa Aesar) were wet mixed in stoichiometric ratios using zirconia jars and balls in a planetary ball mill at 150 rpm for 12 h. Calcination was carried out at 900 °C for 3h. Calcined powder was mixed with 5% polyvinyl alcohol solution and pressed into pellets under uniaxial pressure of 100 MPa followed by cold isotropic pressure of 300M Pa. The pellets were sintered in covered alumina crucibles at 1150 °C for 4 h in air. The density of the sintered pellets, measured by liquid displacement method, was found to be ∼95%. The sintered pellets with diameters of 10–12 mm and thickness of 0.8–1.5 mm were painted with silver paste for electrical contact and poled by applying a DC field of 70 kV/cm for 30 min at room temperature. Direct piezoelectric

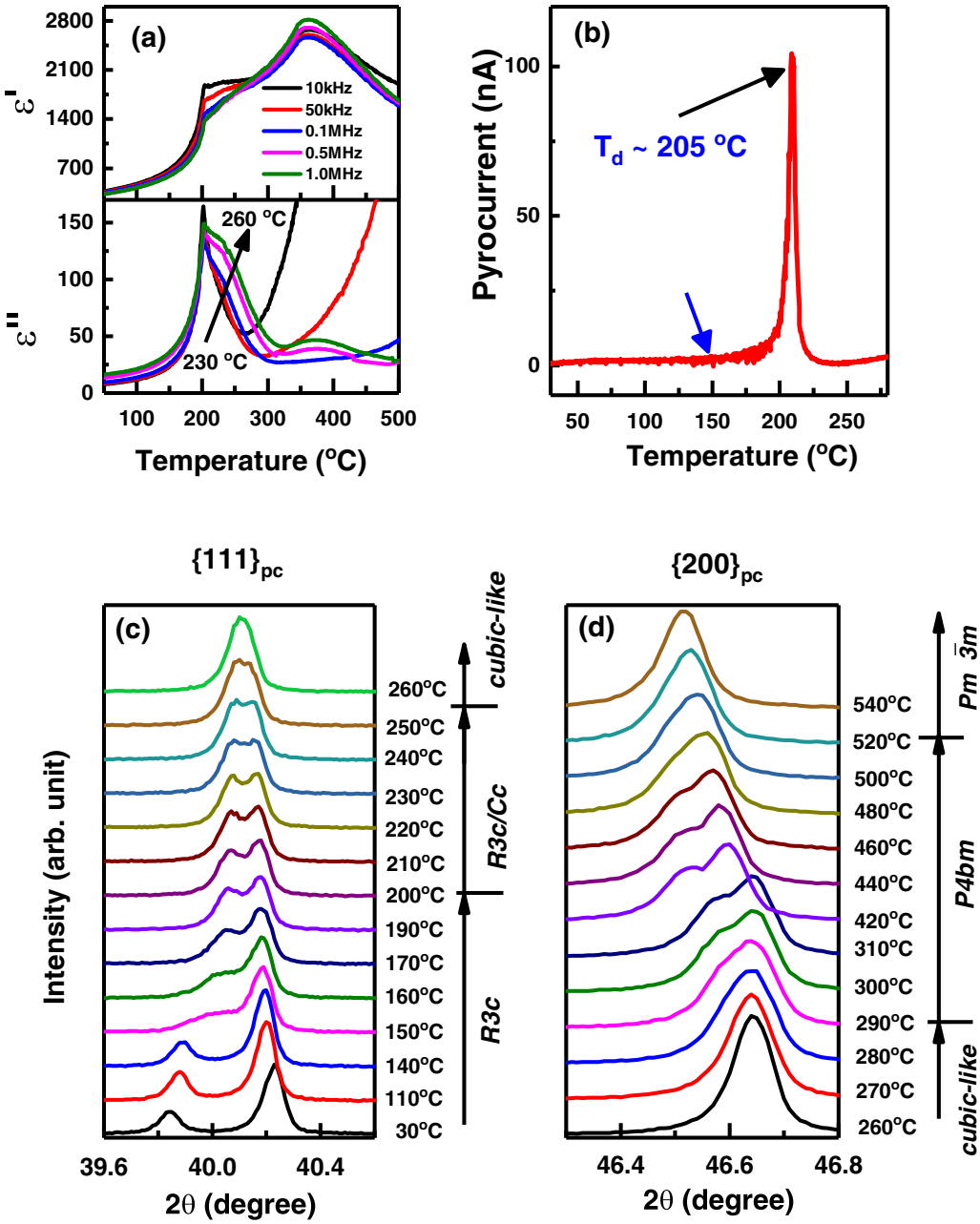

FIG. 1. (a) Temperature dependence of the real and imaginary parts of relative permittivity of poled NBT. (b) Temperature variation of the pyrocurrent. The sharp peak at 205 °C corresponds to the depolarization temperature, T_d. (c) Temperature evolution of the $\{111\}_{pc}$ x-ray Bragg profile of poled and powdered NBT. (d) Evolution of $\{200\}_{pc}$ of poled NBT for $T \geqslant 260$ °C. The split in this profile at 300 °C and above suggests tetragonal distortion corresponding to the *P*4*bm* phase (see Fig. S1).

coefficient (d_{33}) was measured using Piezotest, PM300 with applied force 0.25 N and frequency 110 Hz. Thermal depoling current measurements were carried out using an Electrometer (Keithley, 6514) by heating poled pellets at 3 °C/min. X-ray powder diffraction (XRPD) was carried out using a Rigaku Smartlab x-ray diffractometer with monochromatic Cu $K\alpha_1$ radiation. XRPD and neutron powder-diffraction (NPD) measurements of the poled specimens were carried out after crushing the poled pellets gently to powder. The powder specimens were obtained after grinding the poled pellets. This approach offers texture-free diffraction pattern while at the same time preserves the structural changes caused by the poling field on the global scale. The XRPD patterns of the unpoled specimens were collected after annealing the ground powder at 750 °C for 2 h to remove the effect of residual stress incurred during the grinding process. High-temperature XRPD data were collected on powders of poled pellets. High-temperature dielectric measurements were carried out on poled pellets on heating and then cooling using a Novocontrol Alpha-A impedance analyzer. Room-temperature NPD data were collected at the diffractometer SPODI at FRM-II, Germany (wavelength of 1.548 150 Å) [60]. High-temperature NPD measurements were carried out on poled powders during heating (maximum temperature 600 °C) and cooling. Struc-

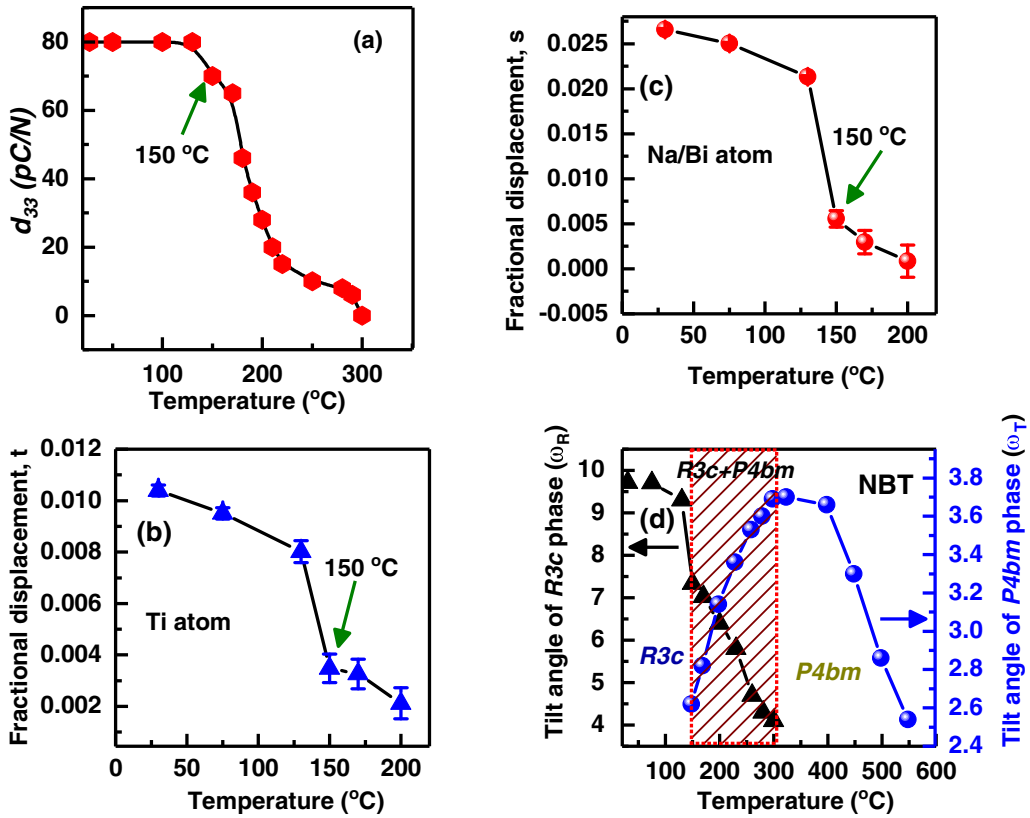

FIG. 2. (a) Variation of d_{33} as a function of annealing temperature of poled NBT. Temperature variation of (b) polar shift (t) of Ti, (c) polar shift (s) of the Na/Bi, (d) antiphase and in-phase octahedral tilts of the *R*3*c* and *P*4*bm* phases phase of NBT. Note the abrupt decrease of the polar shifts and octahedral tilt angle of the *R*3*c* at 150 °C.

tural analysis was performed by the Rietveld method using the FULLPROF package [61].

III. RESULTS AND DISCUSSION

A. Depoling of $x = 0.0$

Figure 1(a) shows the temperature variation of the real and imaginary parts of the relative permittivity of poled NBT ($x = 0$) at different frequencies. A significant dispersion can be seen at ∼205 °C. Thermal depoling current shows a sharp peak at the same temperature [Fig. 1(b)]. Because of the ease in identifying a peak, we have used the temperature corresponding to the peak in the thermal depoling current to characterize the depolarization temperature (T_d) of all compositions in the present work. Figure 1(c) shows the temperature evolution of the pseudocubic $\{111\}_{pc}$ Bragg profile of poled and ground NBT pellets. The breaking of poled pellet to powder removes the preferred orientation effect in the powder-diffraction pattern while retaining the crucial information pertaining to the field-induced changes in the average structure [19,62–64]. This strategy helps in unambiguous analysis of the nature of structural changes accompanying the depoling phenomenon. As reported before [43,48], poling makes the structure appear rhombohedral on the global scale with neatly split $\{111\}_{pc}$ pseudocubic x-ray Bragg profile into a doublet. On heating, the separation between the split peaks decreases gradually, suggesting a gradual decrease in the rhombohedral distortion [Fig. 1(c)]. An abrupt change in the shape of the $\{111\}_{pc}$ Bragg profile, however, can be noted above 140 °C—a new peak appears in between the rhombohedral $\{111\}_{pc}$ doublets. A careful look at the variation of d_{33} vs thermal aging temperature [Fig. 2(a)] suggests that thermal depoling is initiated around the same temperature (∼140 °C). This temperature nearly coincides with the onset of thermal depoling pointed out by Aksel *et al.* [45,47]. However, they failed to notice any distinct structural change presumably because unpoled specimen (the average structure of which is *Cc*) was used in the structural analysis. The dramatic change in the shape of the fundamental x-ray Bragg profiles of poled NBT almost coincides with the onset of the weak superlattice peaks corresponding to in-phase octahedral tilt in the NPD reported earlier [48] (Supplemental Fig. S1 [65]). Though the depoling of NBT starts above 140 °C, the system retains the memory of poling until ∼300 °C, Fig. S2 [65]. The depoling of NBT therefore happens over a large temperature range 150–300 °C, with T_d (∼205 °C) lying in between.

For better appreciation of the structural factors associated with the onset of depoling of NBT, we analyzed the temperature dependence of the structural parameters of poled NBT by Rietveld analysis of NPD data (Figs. S3–S5 in Supplemental Material [65]). For the sake of convenience, we followed the structural description of Megaw and Darlington [66] to describe the rhombohedral (*R*3*c*) phase as it offers direct estimation of the polar cation displacement (*s*), octahedral strain, and octahedral tilt angle [66,67] (for more

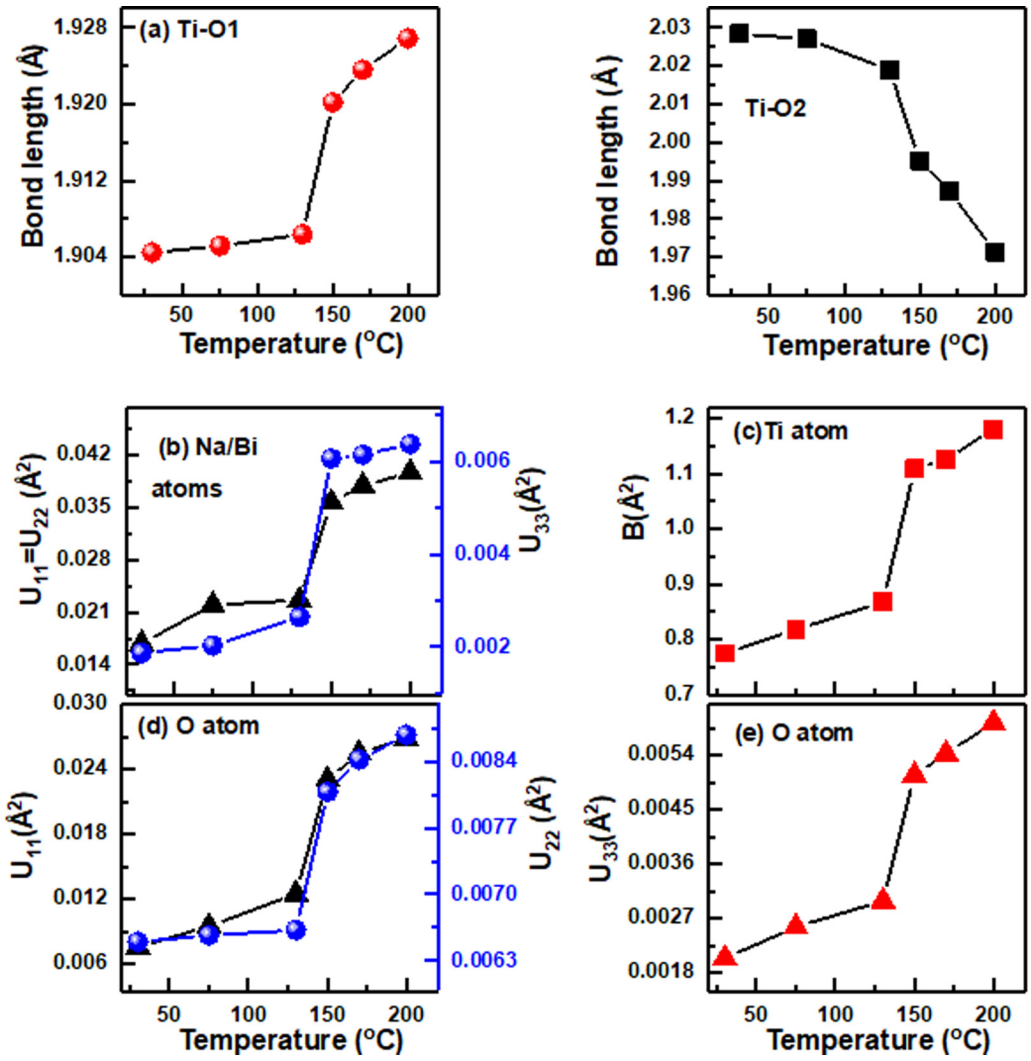

FIG. 3. Temperature dependence of Ti-O bond lengths are shown in (a).Temperature variation of anisotropic thermal parameters of (b) Na/Bi atoms, (c) isotropic thermal parameters of Ti atoms, and (d), (e) anisotropic thermal parameters of O atoms of NBT. These parameters were obtained by Rietveld fits of the NPD patterns. Note the abrupt change in the thermal parameters and bond lengths at 150 °C while system still exhibits predominantly rhombohedral structure.

information please refer to Table S1 in Ref. [65]). During the refinement, site occupancies were fixed as per the nominal composition. The background was modeled with linear interpolation between selected points. Since the isotropic displacement parameters (B) of Na/Bi and O were found to be significantly large ($\sim$4 Å^2), we chose to refine the anisotropic displacement parameters (U) of these atoms. Although the $R3c$ symmetry allowed three independent U ($U_{11} = U_{22}$, U_{33}, and U_{12}) for Na/Bi, and six independent U for the O, we refined only the diagonal elements of the U tensor to reduce the number of refinable structural variables. For Ti, we refined only the isotropic displacement parameter (B). For the sake of consistency, the refinement was carried out in a sequential manner. That is, the final refined parameters of the lower temperature were fed as the initial parameters to fit the NPD pattern of NBT of the next high temperature. The refined structural parameters of NBT for some representative temperatures are given in Tables S3 and S4 in Ref. [65]. As evident from Figs. 2(b) and 2(c), the polar displacements of both Na/Bi and Ti, antiphase octahedral tilt angle [Fig. 2(d)] show abrupt decrease at $\sim$150 °C. The abrupt increase in the Ti-O_1 and decrease in Ti-O_2 bonds (for details of the nomenclature of the atoms please refer to the schematic diagram Fig. S6 in Ref. [65]) is another manifestation of considerable decrease in the octahedral distortion, Fig. 3(a). The sudden increase in the atomic displacement parameters of all the atoms at 150 °C [Figs. 3(b)–3(e)] suggests that the notable decrease in the average polarization of the $R3c$ phase is accompanied by a significant increase in structural disorder. This disorder is triggered by the onset of the $P4bm$ phase in the $R3c$ matrix (Fig. S1 in Ref. [65]). Because of the importance of this structural event in initiating the depoling process, we have given the corresponding temperature a special notation T_2'. While our analysis confirms that the initiation of the depoling process is triggered by a structural event at $\sim$150 °C, it was not possible to associate any special structural event with the depolarization temperature $T_d \sim 205$ °C, which lies between T_2 and T_2'.

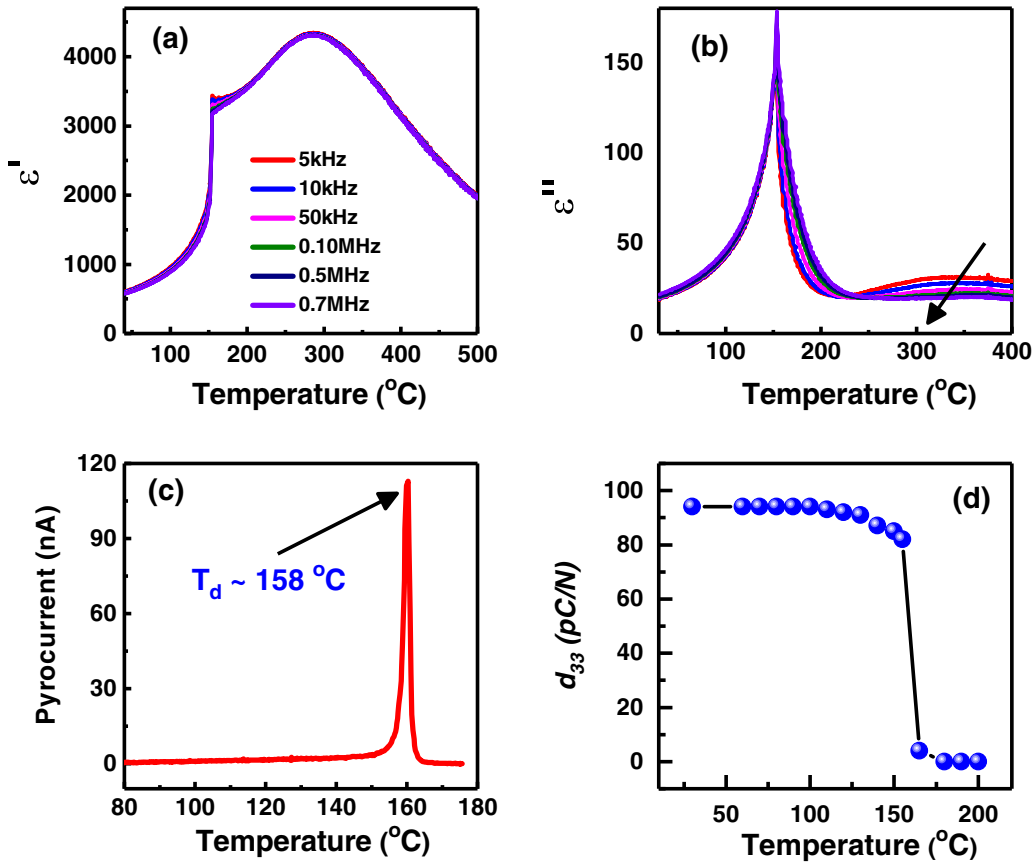

FIG. 4. Temperature dependence of the real (a) and imaginary (b) part of relative permittivity of poled $x = 0.04$ at different frequencies. The arrow shows increasing frequency. (c) Temperature dependence of the depolarization current. The sharp peak at $T_d \sim 158\,^{\circ}\mathrm{C}$ in (c) characterizes the depolarization temperature. (d) Variation of d_{33} vs annealing temperature of poled $x = 0.04$.

B. Depoling of $x = 0.04$

This composition is representative of the range $0.03 \leqslant x \leqslant 0.05$ which exhibits two distinctive features: conversion of Cc to $R3c$ (in unpoled specimens) [22] and overlap of T_d and T_2 [46]. The depolarization temperature of $x = 0.04$ is 158 °C [Figs. 4(a)–4(c)]. In contrast to $x = 0$ which depoles in a large temperature interval (150–300 °C), complete depoling of $x = 0.04$ occurs in a significantly narrow interval 150–160 °C, Fig. 4(d). Consistent with this, the rhombohedral distortion, measured as 90°-α (where α is the rhombohedral angle), abruptly drops to zero, suggesting transition to a cubic structure at 160 °C, Figs. 5(a) and 5(b). Neutron powder-diffraction patterns, on the other hand, show weak superlattice peaks corresponding to in-phase octahedral tilt at these temperature, Fig. 5(c). These superlattice peaks could be nicely accounted for by the $P4bm$ model, Figs. S7(c) and S7(d) [65]. Thus, what appears as a cubic phase in the XRD pattern is $P4bm$ phase with a cubiclike metric; the $P4bm$ transforms to cubic ($Pm\bar{3}m$) above 330 °C. Rietveld fits of the NPD patterns and refined structural parameters of poled $x = 0.04$ for some representative temperatures is given in Fig. S7 and Table S6, Ref. [65]. The polar cation displacement (Fig. S8 [65]), the antiphase octahedral tilt angle [Fig. 5(d)], thermal parameters (Figs. S9(a)–S9(d) [65]), and bond lengths [Figs. S9(e) and S9(f) [65]) all show smooth variation with temperature up to 150 °C. At 160 °C, the NPD pattern can be fitted with $P4bm$ structural model. As a double check, we also investigated the propensity to retain the structural memory of the poling effect by analyzing the XRD pattern after thermal annealing of poled $x = 0.04$ at different temperatures. The XRD pattern of the specimen annealed at 160 °C was found to be the same as that of unpoled specimens (Fig. S10 [65]), confirming that the system has lost its poling memory when heated at 160 °C. Accordingly, we fix the T_2 for $x = 0.04$ as ∼160 °C. Since our neutron-diffraction data were collected at relatively larger temperature intervals (20 °C), we could not capture T_2' (the temperature corresponding to the first appearance of the $P4bm$ phase within the $R3c$ matrix). It is expected to lie somewhere between 150 and 160 °C. Based on this observation, the maximum difference between T_2 and T_2' (i.e., $T_2 - T_2'$) is ∼10 °C. Since the thermal depolarization temperature T_d has to lie in between T_2' and T_2, it would appear to coincide with T_2 (as in the phase diagram of Ref. [46], and also in Fig. 11 of the present work).

We sought to understand the remarkable decrease in the difference T_2-T_2' (from T_2-$T_2' \sim 150\,^{\circ}\mathrm{C}$ for $x = 0$ to T_2-$T_2' \sim 10\,^{\circ}\mathrm{C}$ for $x = 0.04$) and the consequent overlap of T_d and T_2 in the composition range $0.03 \leqslant x \leqslant 0.05$ [46] in terms of the kinetics of the $R3c$-$P4bm$ transformation. Figure 6(a) shows the temperature dependence of the tetragonality (c/a-1) of the high-temperature $P4bm$ phase of compositions in the range $0.00 \leqslant x \leqslant 0.03$. Given the better resolution of the XRD data as compared to the NPD data, the tetragonality was determined using lattice parameters obtained from the

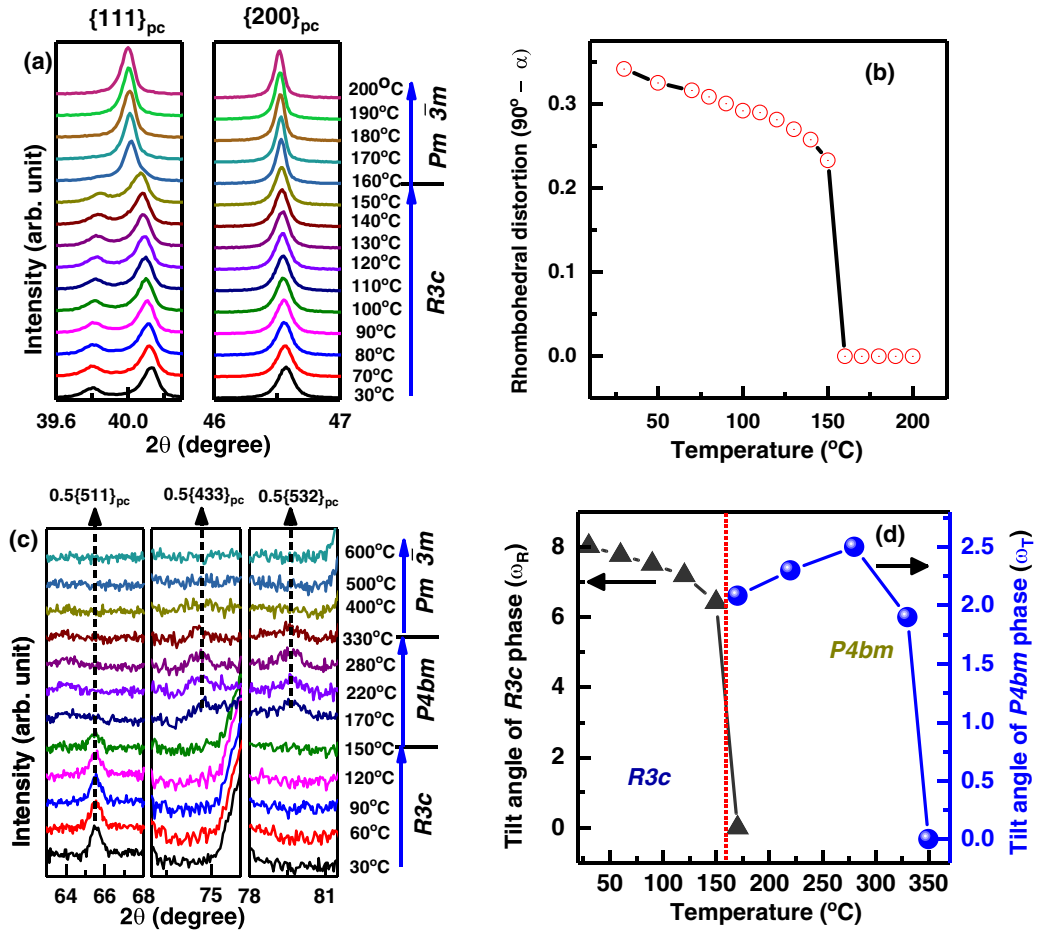

FIG. 5. (a) Temperature evolution of the $\{111\}_{pc}$ and $\{200\}_{pc}$ x-ray Bragg profiles of poled and ground $x = 0.04$. (b) Temperature variation of the rhombohedral distortion 90°-α, where α is the rhombohedral angle derived from the hexagonal lattice parameters of the *R*3*c* phase. (c) Temperature evolution of selected superlattice peaks in the neutron powder-diffraction pattern of poled $x = 0.04$. (d) Temperature dependence of antiphase tilt angle (ω_R) of *R*3*c* and in-phase tilt angle (ω_T) of the *P*4*bm* phase, respectively, of NBT-0.04BT. These structural parameters were obtained by Rietveld fitting of the NPD patterns of NBT-0.04BT.

high-temperature XRD measurements of poled and ground powder specimens. A noticeable spontaneous tetragonal strain ($c/a > 1$) is evident for all $x \leqslant 0.02$, Fig. 6(a). The spontaneous strain collapses for $x = 0.03$ and $x = 0.04$. We argue that the collapse of tetragonality considerably reduces the transformation strain and the associated kinetic barrier for the *P*4*bm*-*R*3*c* transformation. Viewed in this light, the dramatic reduction of T_2-T_2' for the compositions $0.03 \leqslant x \leqslant 0.05$ is attributed to the ability of the system to complete the *R*3*c*-*P*4*bm* transformation without the need for excessive superheating (when compared with, say, NBT)

C. The *Cc*/*R*3*c* boundary at $x = 0.03$

Figure 6(b) shows neutron powder-diffraction patterns of unpoled NBT-BT as a function of composition at close intervals. It is interesting to note that the superlattice peaks corresponding to the in-phase octahedral tilt first appear at $x = 0.03$, the same composition at which *Cc*/*R*3*c* boundary was reported by Ma *et al.* [22]. Levin and Reaney [57] have argued that the *Cc* average structure is a result of coherent assemblages of nanometer-sized regions of in-phase octahedral tilt and relatively larger regions of $a^-a^-a^-$ antiphase tilt. The absence of the *P*4*bm* superlattice peaks in the NPD pattern for $x < 0.03$ suggests that the coherence length/volume fraction of the in-phase tilted region is not large enough to diffract the neutron beams. Once they grow reasonably large, they acquire a separate identity as the *P*4*bm* phase, breaking the very foundation of the average *Cc* structure. We may represent this phenomenon as $Cc \rightarrow R3c + P4bm$. Our observation provides a rationale of the *Cc*/*R*3*c* boundary at $x = 0.03$ reported earlier [22]. It is important to note that although poling suppresses the *P*4*bm* phase on the global scale for $0.03 \leqslant x \leqslant 0.06$ [Figs. 6(c) and 6(d)], its implication can still be seen from the fact that the rhombohedral distortion [Fig. 6(e)] and the depolarization temperature [Fig. 6(f)] starts decreasing only for $x \geqslant 0.03$.

D. Depoling of $x = 0.06$

Thermal depoling current measurement of poled $x = 0.06$ suggests its $T_d \sim 116\,^\circ$C, Fig. 7. However, a noticeable decrease in d_{33} can be seen above $70\,^\circ$C, well below T_d [Fig. 7(d)]. A careful look at the depoling current vs temperature plot reveals a steady increase in current above $70\,^\circ$C. To identify the structural mechanisms, if any, associated with

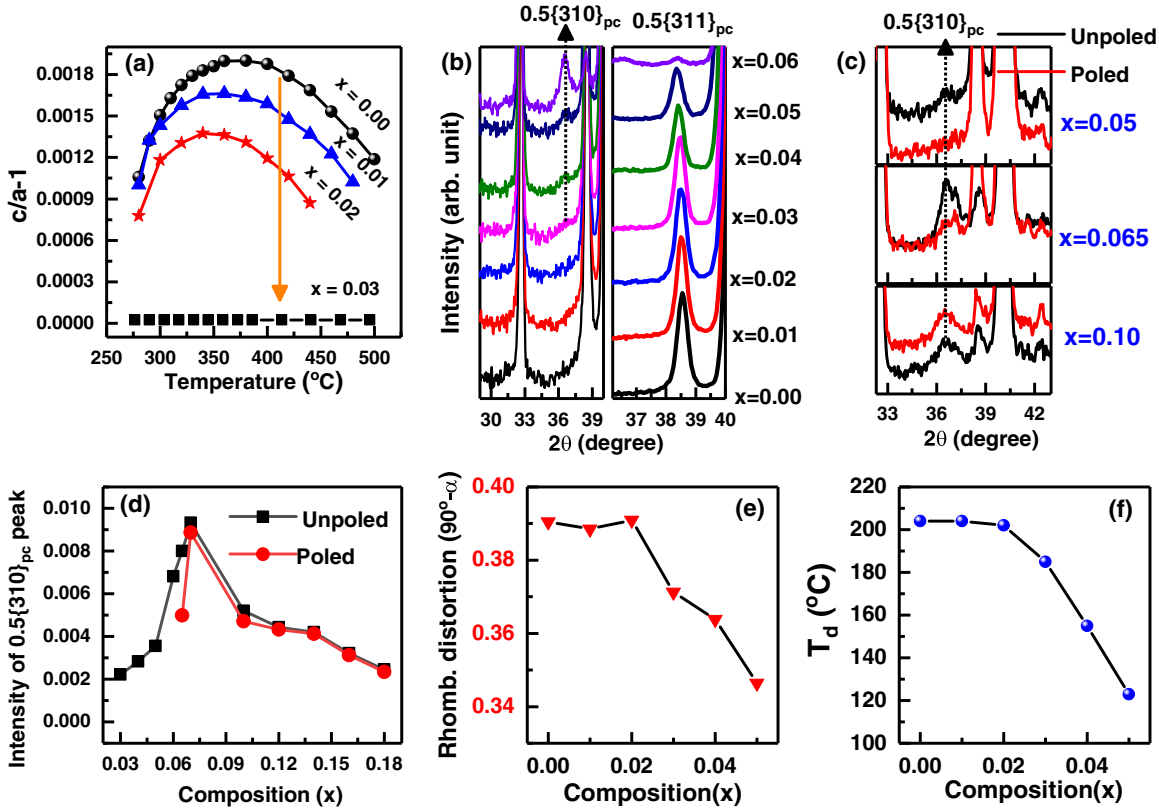

FIG. 6. (a) Temperature dependence of the tetragonality (c/a-1) of the intermediate high-temperature tetragonal ($P4bm$) phase of (1-x)NBT-(x)BT as determined from temperature-dependent XRD measurements. (b) Composition evolution of the $0.5\{310\}_{pc}$ and $0.5\{311\}_{pc}$ superlattice reflections in the NPD patterns of unpoled NBT-xBT. (c) Comparison of unpoled and poled NPD patterns of $x = 0.05$, $x = 0.065$, and $x = 0.10$ highlighting the effect of poling on the superlattice peaks. (d) Composition dependence of the integrated intensity of the $0.5\{310\}_{pc}$ superlattice peak in the NPD patterns of unpoled and poled specimens. (e) Composition dependence of the rhombohedral distortion ($90°$-α) derived from the lattice parameters of poled NBT-BT. The composition dependence of the depolarization temperature (T_d) is shown in (f).

the two distinctive changes at 75 °C and 116 °C, we performed temperature-dependent XRD and NPD studies on poled and ground $x = 0.06$. Consistent with the previous studies [19,20,53,68], the structure of poled $x = 0.06$ at room temperature is $R3c$, Figs. 8(a) and 8(b). On heating, poled $x = 0.06$ shows emergence of a $P4mm$-like ferroelectric distortion at ∼55 °C (Fig. 8(a), Fig. S11 [65]). NPD study revealed that the onset of the ferroelectric $P4mm$ distortion is also accompanied by the appearance of superlattice peaks corresponding to the $P4bm$ phase, Figs. 8(b) and 8(c). In contrast to $x < 0.06$ for which depoling begins at the onset of the $P4bm$ phase (i.e., at T_2'), the onset of the $P4bm$ phase does not depole $x = 0.06$. It appears that the accompanying $P4mm$ ferroelectric distortion prevents the depoling at T_2'. Depoling rather begins above 70 °C, i.e., when the $R3c$ phase vanishes (at T_2). Incidentally, T_2 coincides with the temperature corresponding to the onset of detexturing of ferroelectric domains in poled $x = 0.06$, reported earlier by Jo *et al.* [58,59]. Above T_2, the ferroelectric order is sustained by the emergent ferroelectric $P4mm$ phase which survives up to 115 °C (we denote this temperature as T''). The depolarization temperature T_d of $x = 0.06$ nearly coincides with T''. It is important to note that although the ferroelectric $P4mm$ distortion and the in-phase octahedral tilt appear at almost the same temperature (∼55 °C) for poled $x = 0.06$, the survival of the in-phase octahedral tilt well above T'' confirms that these two distortions are not coupled. The $P4bm$ phase of $x = 0.06$ disappears above 300 °C.

E. Depoling of $x \geqslant 0.065$

We also investigated poled $x = 0.065$, a composition adjacent to $x = 0.06$. The XRD pattern of poled $x = 0.065$ suggests a coexistence of $R3c$ and $P4mm$ distortions at room temperature (Fig. S12(a) [65]). In contrast to $x = 0.06$, the NPD pattern of poled $x = 0.065$ shows superlattice peaks corresponding to the $P4bm$ phase (although the intensity is reduced when compared with unpoled $x = 0.065$), Figs. 6(c) and 6(d). Depoling current measurement of this composition reveals a small broad peak at ∼90 °C, followed by a sharp peak at $T_d \sim 148$ °C (Fig. S12(c) [65]). Consistent with this, d_{33} decreases (on thermal aging) in a two-step process—a gradual decrease just above 90 °C, followed by a sharp drop at T_d (Fig. S12(d) [65]). The $R3c$ phase vanishes completely somewhere between 80 and 90 °C (Fig. S13 in Ref. [65]) confirming that (as for $x = 0.06$) the onset of thermal depoling coincides with T_2. The ferroelectric $P4mm$ distortion gradually transforms to cubic over a temperature range 140–180 °C for this composition.

We also investigated a composition $x = 0.10$ away from the MPB. This composition does not exhibit the rhombohedral ($R3c$) phase at room temperature. The XRD pattern sug-

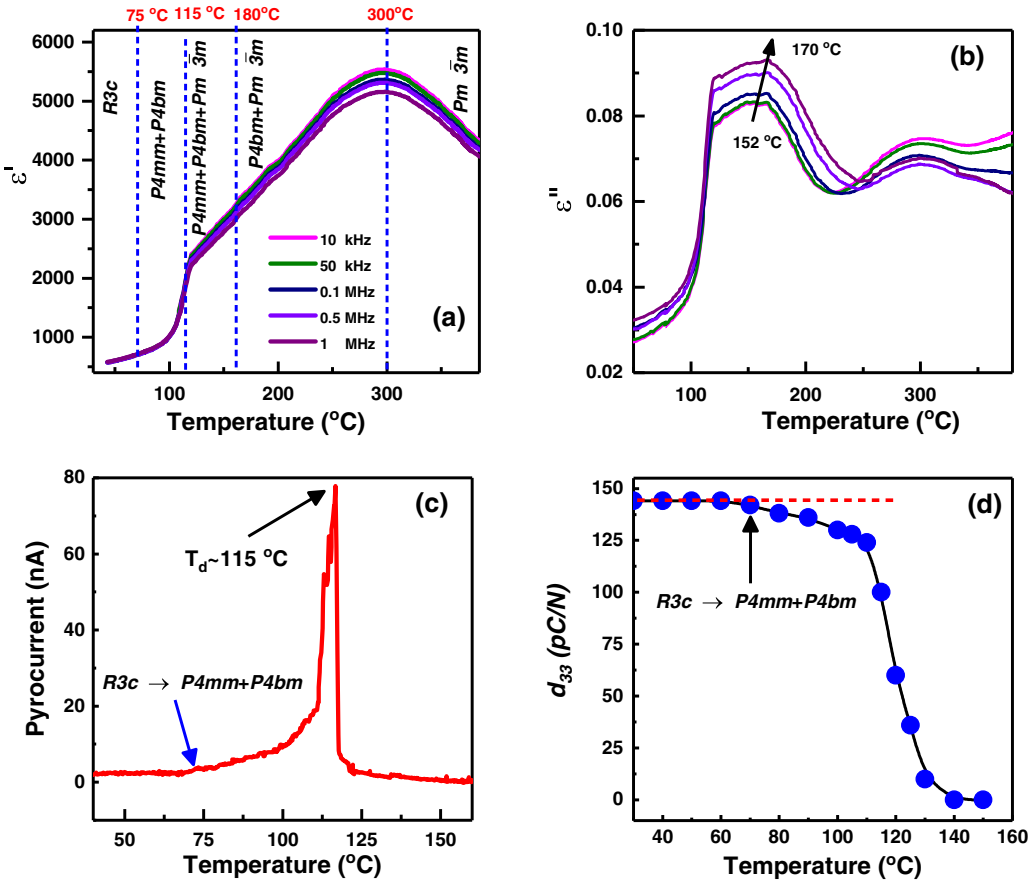

FIG. 7. Temperature dependence of the (a) real and (b) imaginary part of the relative permittivity of poled $x = 0.06$. (c) Temperature variation of the thermal depolarization current. Apart from the sharp peak at 116 °C corresponding to the depolarization temperature, a noticeable increase in the thermal depolarization current can be seen above 70 °C. (d) Variation of d_{33} of poled $x = 0.04$ as a function of annealing temperature. The decrease from the constant value (shown by the dashed line) above 70 °C is consistent with the increase in the thermal depolarization current around the same temperature in (c).

gests tetragonal ($P4mm$) ferroelectric distortion, Fig. S14(a) [65]. However, NPD pattern shows $P4bm$ superlattice peaks [Fig. 6(c)]. This structural state is analogous to that of poled $x = 0.065$ above 80 °C. Depoling current measurement of $x = 0.10$ shows only one peak at $T_d = 185$ °C, Fig. S14(b) [65]. Like $x = 0.065$, the $P4mm \rightarrow Pm\bar{3}m$ transformation in $x = 0.10$ occurs over a reasonably wide temperature range 170–220 °C, Fig. S14(a) [65]. For still higher compositions, say $x \geqslant 0.20$, which exhibit only tetragonal ($P4mm$) distortion and no in-phase octahedral tilt (Fig. S15(a) in Ref. [65]), depoling occurs in a significantly narrow temperature interval (Fig S15(b) [65]), as in normal ferroelectrics. It is apparent that for $0.065 \leqslant x \leqslant 0.18$ the pervading in-phase tilt is responsible for making the $P4mm$ distortion disappear over an extended temperature range and help sustain the memory of the poling above T_d.

F. A note on $T_{VF} < T_d$

Although, at present we have no clue to explain, it is worth highlighting an interesting difference regarding the relaxor ferroelectric behavior of NBT and its derivatives *vis-à-vis* the classical relaxor ferroelectric systems like $Pb(Mg_{1/3}Nb_{2/3})O_3$ (PMN), (Pb, La)(Zr, Ti)O_3 (PLZT), etc. [69–77]. In Table I we compare the Vogel-Fulcher temperature (T_{VF}) of some representative compositions of NBT-BT (Fig. 9) and their respective T_d. T_{VF} was determined following the Vogel-Fulcher analysis $f = f_0 \exp[-E_a/k_b(T''_m - T_{VF})]$, of the frequency ($f$) dependence of T''_m, the temperature at which the imaginary part of the permittivity exhibits maximum [75]. E_a is the activation energy. It is generally believed that the dynamic polar nanoregions freeze below T_{VF}. For the sake of direct comparison, we show in Table II the reported T_{VF} and T_d for some conventional relaxor ferroelectrics systems. For these systems, T_{VF} is the same as T_d [69–77]. In contrast, for the NBT-xBT ($0 \leqslant x \leqslant 0.18$) T_d is invariably higher than

TABLE I. Vogel-Fulcher temperatures (T_{VF}), depolarization temperature (T_d), and activation energy (E_a) of (1-x)NBT-xBT.

Composition (x)	T_{VF} (in °C)	Depolarization temperature (T_d) in °C	Activation energy (E_a) in meV
0.00	192	205	1.9
0.04	107	155	10.3
0.06	95	110	14.1
0.10	170	185	16.4

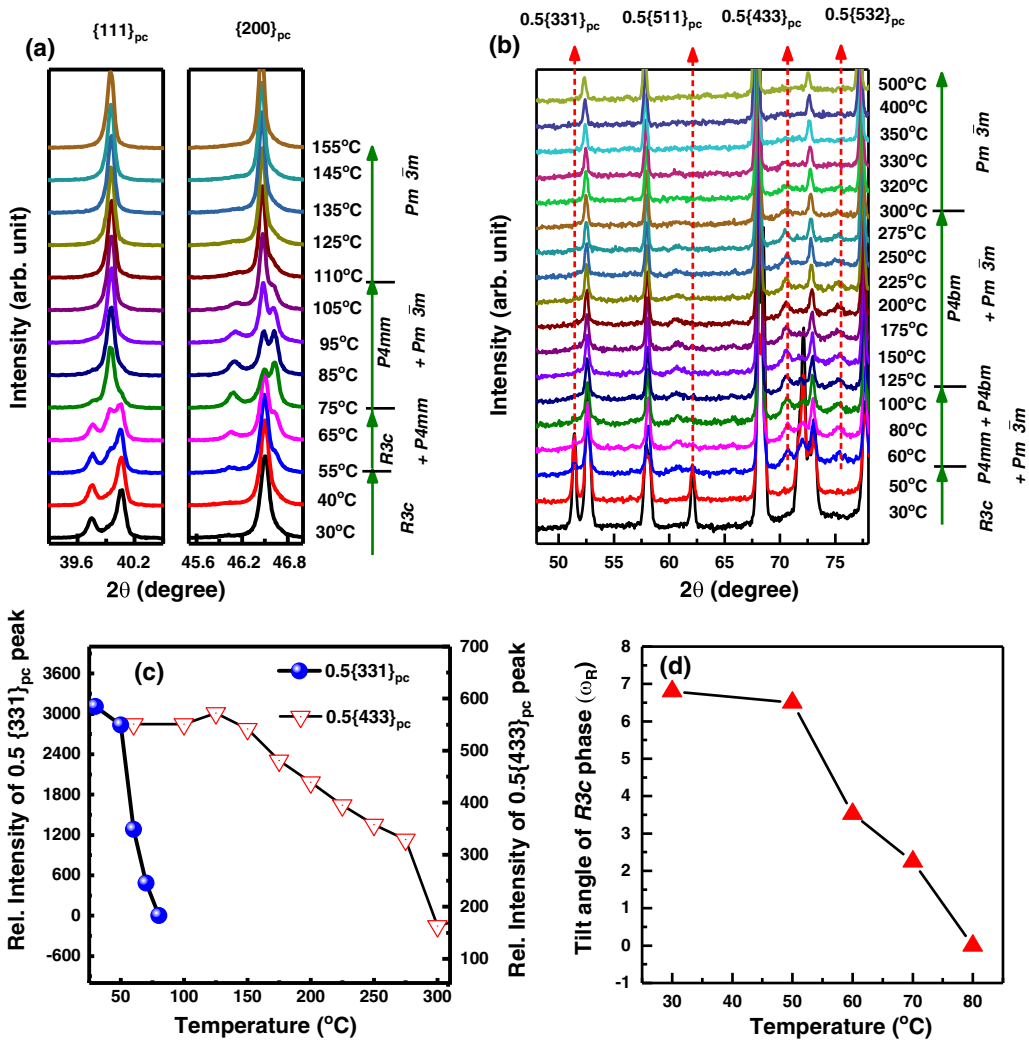

FIG. 8. (a) Evolution of the $\{111\}_{pc}$ and $\{200\}_{pc}$ X-ray Bragg profiles of poled and ground $x = 0.06$ with increasing temperature. (b) Neutron powder-diffraction pattern in a limited 2θ range to highlight the thermal evolution of the superlattice peaks of poled $x = 0.06$. (c) Temperature variation of the intensity of $0.5\{331\}_{pc}$ (corresponding to the antiphase tilt) and $0.5\{433\}_{pc}$ (corresponding to the in-phase tilt) superlattice peaks. The antiphase tilt associated with the *R*3*c* phase vanishes around 75 °C whereas the in-phase vanishes at 300 °C. (d) Tilt angle of *R*3*c* phase as a function of temperature. Note the abrupt change in antiphase tilt angle above 50 °C due to onset of in-phase octahedral tilt.

T_{VF}. This unique discrepancy appears to suggest that the nature of relaxor behavior in NBT-BT is qualitatively different from those of the conventional classical relaxor ferroelectric systems. The origin for this difference may be sought in the qualitative different nature of random fields imparting relaxor characteristic to NBT (and its derivatives) *vis-à-vis* the conventional relaxor ferroelectric systems. The random fields disrupting the onset of long-range ferroelectric order in most other relaxor ferroelectric systems are associated with point defects on the regular lattice site of the structure [78–83]. For example, in the case of $Pb(Mg_{1/3}Nb_{2/3})O_3$ (PMN) the random field is attributed to the lack of electroneutrality on the local scale due to divalent (Mg^{+2}) and pentavalent (Nb^{+5}) ions occupying the same lattice sites [79–82]. Similarly, local defect dipoles become the source of random field when tetravalent La^{+3} partially replaces divalent Pb^{+2} ions in $PbTiO_3$ or PZT [72,82,83]. While ions with two different valence states (Na^{+1} and Bi^{+3}) occupy the same crystallographic site in NBT and can be an intrinsic source of random field (like in PMN), the presence of ferroelectric incompatible in-phase octahedral tilt on the mesoscopic length scale is an additional factor which appears to primarily determine the relaxor nature of NBT-based ferroelectrics. For most compositions, since these in-phase tilted regions precede the development of ferroelectric order as the system is cooled from the cubic paraelectric state, they prevent the development of the long-range ferroelectric order. This may be a possible reason for the anomalous feature $T_d > T_{VF}$ in NBT-based ferroelectric systems.

G. Phase diagram: Poled specimens

We have incorporated the results presented here to create an updated phase diagram for NBT-BT, Fig. 10. Among the composition-temperature phase diagrams reported for NBT-BT [17,22,46,84], the phase diagram reported by

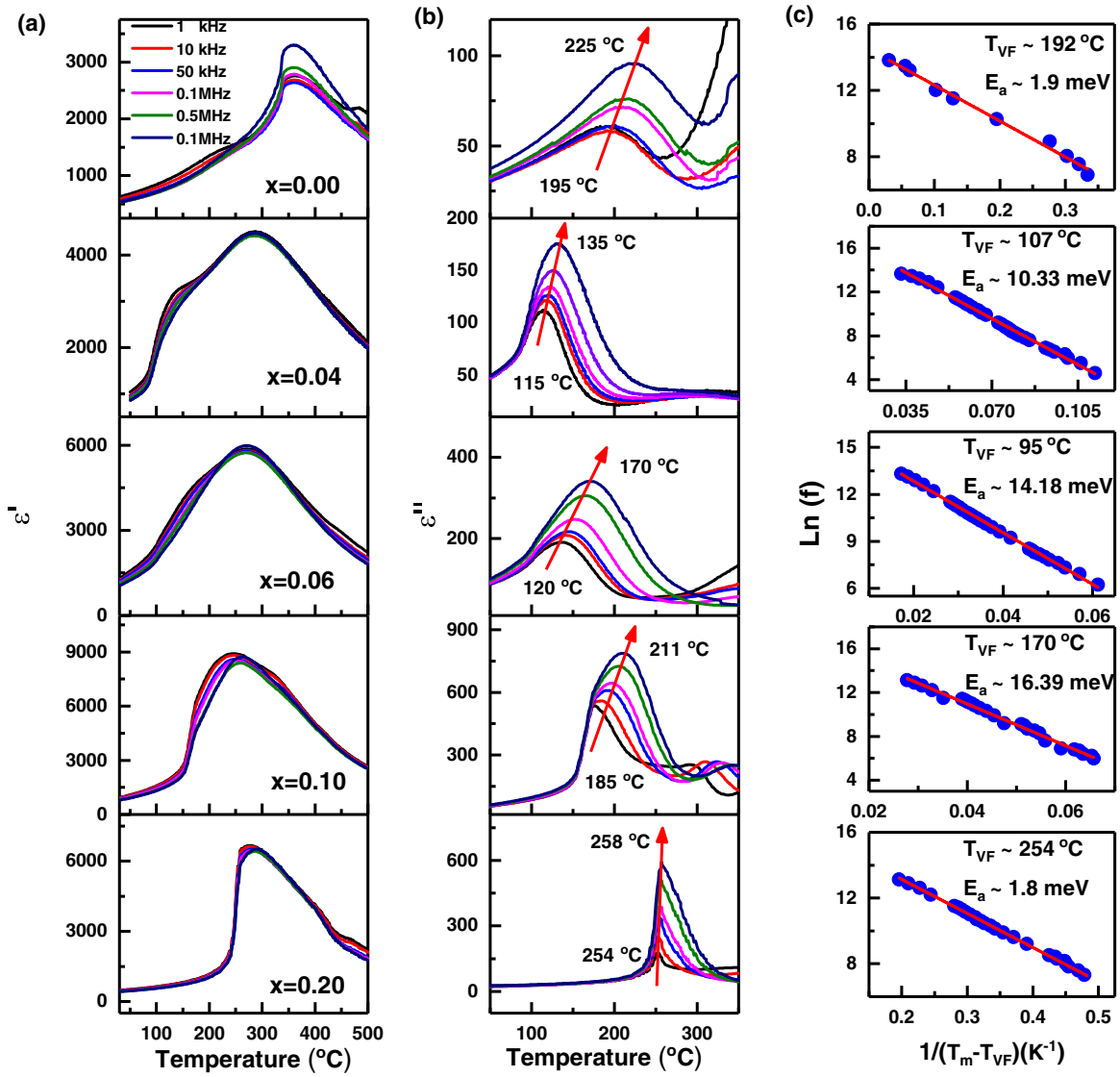

FIG. 9. Temperature variation of the (a) real (ε') and (b) imaginary part (ε'') of unpoled (1-x)NBT-xBT at different frequencies. The arrows show increasing frequency. (c) Vogel Fulcher fits of the data derived from the ε'' (f, T) of the different compositions.

Cordero *et al.* [46] is most extensive. It shows six characteristic temperatures: T_m (dielectric maximum temperature), T_{me} (maximum temperature), T_d (thermal depolarization temperature), T_1 ($P4bm$-$Pm\bar{3}m$ transition temperature), T_2 ($P4bm$-$R3c$ transition temperature), and T_3 (unidentified). In this phase diagram, the T_1 (x) line ends abruptly at $x = 0.05$, the reason for which has not been specified [46]. For the sake of consistency, the notations T_1 and T_2 representing $P4bm$-$Pm\bar{3}m$ and $P4bm$-$R3c$ transition temperatures, respectively, are borrowed from the phase diagram reported earlier by Cordero *et al.* [46]. However, the data points representing these lines in Fig. 10 are based on our work. Since the initiation of thermal depoling in $x \leqslant 0.05$ is triggered by the onset of the $P4bm$ phase in the $R3c$ matrix, we have introduced this as an additional characteristic temperature (T_2') in our phase diagram. The $R3c$ and the $P4bm$

TABLE II. Vogel-Fulcher temperatures (T_{VF}) and depolarization temperature (T_d) for representative canonical relaxor ferroelectrics.

Canonical relaxor ferroelectrics	T_{VF} (in °C)	Depolarization temperature (T_d) in °C	References
$(Pb_{0.92}La_{0.08})(Zr_{0.65}Ti_{0.35})O_3$ (PLZT 8/65/35)	37	37	[72–74]
$Pb(Mg_{1/3}Nb_{2/3})O_3$ (PMN)	−53	−53	[75,76]
$0.90PbMg_{1/3}Nb_{2/3}O_3$-$0.10PbTiO_3$ (PMN-10PT)	7	7	[69,75]

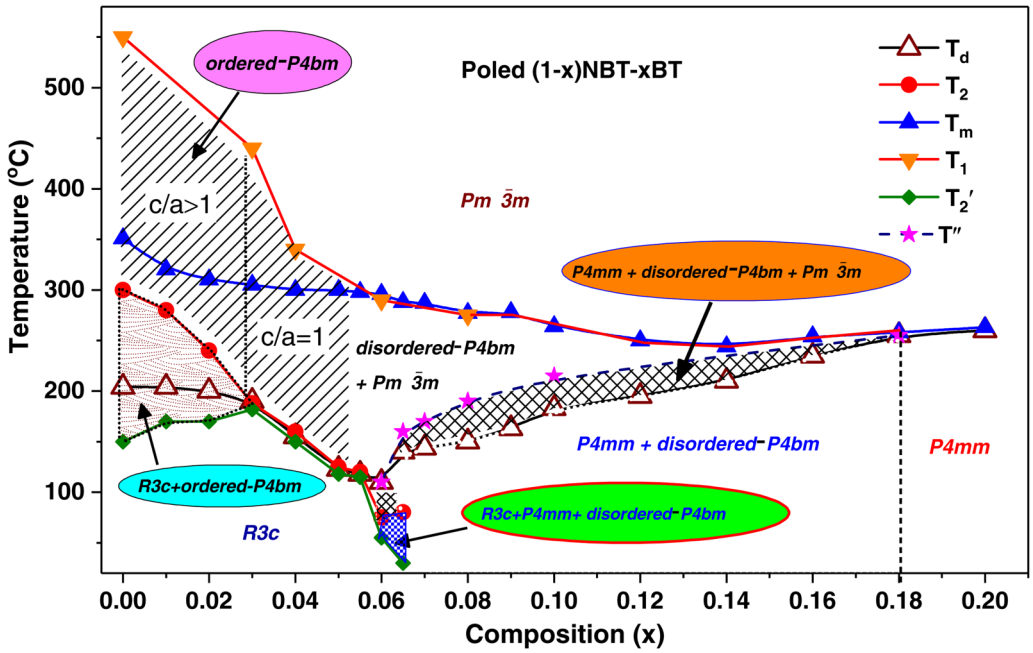

FIG. 10. Phase diagram of poled (1-x)NBT-xBT. $T_d \rightarrow$ depolarization temperature, $T_2 \rightarrow$ rhombohedral $R3c$ to tetragonal $P4bm$ phase transition temperature, $T_m \rightarrow$ the temperature of the dielectric permittivity maximum, $T_1 \rightarrow$ tetragonal $P4bm$ to cubic $Pm\bar{3}m$ transition temperature, $T_2' \rightarrow$ temperature corresponding to the onset of in-phase octahedral tilt, T''→tetragonal ($P4mm$) to cubic ($Pm\bar{3}m$) transition temperature. For details, please refer to the section on phase diagram.

phases coexist between T_2' and T_2. The thermal depolarization temperature (T_d) lies somewhere between T_2' and T_2 and is not associated with any unique structural event for $x < 0.03$. For $0.03 \leqslant x \leqslant 0.05$, the difference between T_2' and T_2 decreases considerably (T_2-$T_2' \sim 10\,^{\circ}$C), giving the impression that T_d (x) coincides with T_2 (x). Since the $R3c$ phase appears only in the composition range $x \leqslant 0.065$, the T_2 (x) line is restricted to $x = 0.065$. We have divided the $P4bm$ phase into two categories: *ordered* $P4bm$ (for $0 \leqslant x \leqslant 0.05$) and *disordered* $P4bm$ ($0.06 \leqslant x < 0.18$). This distinction is based on whether the average $P4bm$ structural model can fit the superlattice peaks in the NPD patterns accurately or not. It turns out that it can fit well for $x \leqslant 0.05$ (Fig. S5 and Figs. S7(b) and S7(c) [65]) but not for $x \geqslant 0.06$ (Fig. S16 and Fig. S17 [65]). The phase diagram also depicts the correlation between the collapse of the tetragonality of the $P4bm$ phase [Fig. 6(a)] and the overlap of T_d and T_2 by drawing a vertical line at $x = 0.03$. The $P4bm$ exhibits tetragonal average lattice distortion (c/a>1) for $x < 0.03$ [Fig. 1(d)] and cubic metric ($c/a = 1$) for $0.03 \leqslant x \leqslant 0.05$ [Fig. 5(a)]. It is interesting to note that the *disordered* $P4bm$ phase appears only when the system develops long-range $P4mm$ ferroelectric distortion. Levin *et al.* have argued that the in-phase tilt axis is parallel to the nonpolar *a/b*-axis of the $P4mm$ tetragonal distortion [17]. However, on heating, the $P4mm$ distortion disappears at a much lower temperature (T'') than the transformation of the disordered-$P4bm$ phase to cubic. Despite the distinction we make between ordered and disordered $P4bm$ phases, we denote the *disordered* $P4bm$-cubic ($Pm\bar{3}m$) transition temperature with T_1. This helps in drawing the T_1 (x) line beyond $x >$ 0.05 and completing the "missing" information in Ref. [46]. Incidentally, the dielectric maximum temperature T_m nearly coincides with T_1 for all $x \geqslant 0.06$ (Fig. S18 [65]). This is not the case for $x < 0.06$. The disappearance of the *disordered* $P4bm$ phase for $x \geqslant 0.18$ is another additional feature of our phase diagram. From the property point of view, this boundary is associated with depolarization temperature, tetragonality of the $P4mm$ distortion, and the coercive field exhibiting maximum [23]. The phase diagram also highlights a small pocket between $x = 0.06$ and $x = 0.065$ where three phases ($R3c$+*disordered-*$P4bm + P4mm$) coexist.

H. Phase diagram: Unpoled specimens

For the sake of completeness, we also present an updated phase diagram of unpoled NBT-BT, Fig. 11. The important differences *vis-à-vis* the phase diagram of poled NBT-BT (Fig. 10) lie only in the composition range $x < 0.07$. Following Ma *et al.* the Cc phase is shown for $x < 0.03$ [22]. Incorporating the results shown in Fig. 6(b), the average structure of the composition range $0.03 \leqslant x \leqslant 0.05$ at room temperature is shown as $R3c$+*ordered* $P4bm$. We may note that T_2 (temperature corresponding to the disappearance of the $R3c$ phase) is the same for both unpoled and poled specimens, Fig. S19 [65]. Another difference *vis-à-vis* the phase diagram shown in Fig. 10 is the replacement of depolarization temperature T_d in Fig. 11 with the Vogel-Fulcher temperature (T_{VF}), Fig. 9. In contrast to most relaxor ferroelectric wherein T_{VF} and T_d almost coincide, T_d is considerably larger than T_{VF} for NBT-based relaxor ferroelectrics (Tables I and II).

IV. CONCLUSIONS

We shed light on the fundamental structural mechanisms governing thermal depoling processes in the lead-free piezoelectric system (1-x)$Na_{0.5}Bi_{0.5}TiO_3$-(x)$BaTiO_3$. We show that

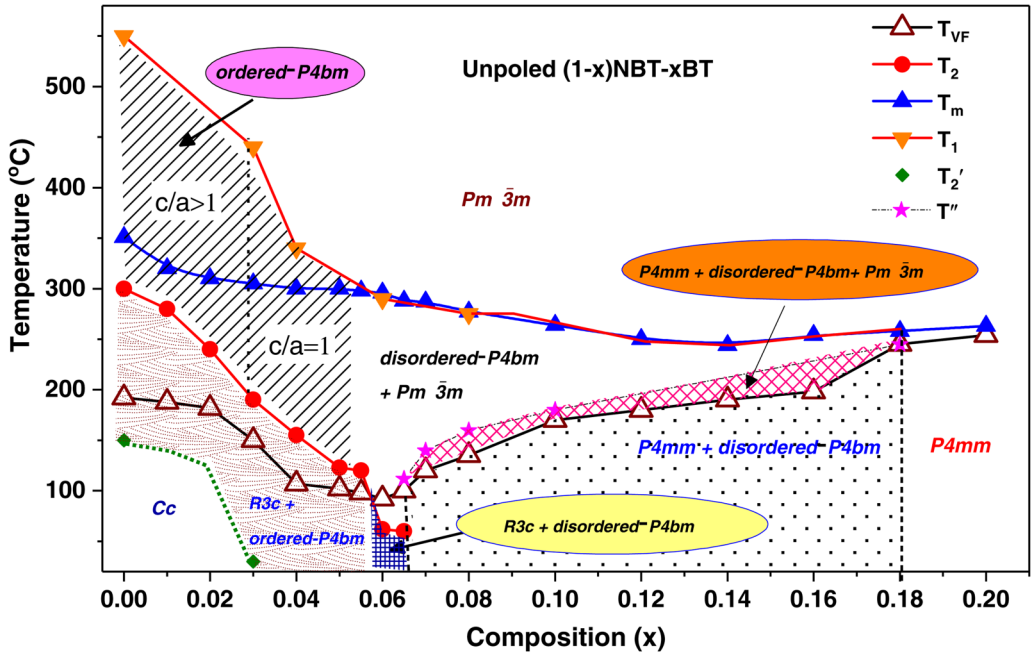

FIG. 11. Phase diagram of unpoled (1-x)NBT-xBT. $T_{VF} \rightarrow$ Vogel-Fulcher temperature (freezing temperature), $T_2 \rightarrow$ rhombohedral $R3c$ to tetragonal $P4bm$ phase transition temperature, $T_m \rightarrow$ the temperature of the dielectric permittivity maximum, $T_1 \rightarrow$ tetragonal $P4bm$ to cubic $Pm\bar{3}m$ transition temperature, $T_2' \rightarrow$ temperature corresponding to the onset of in-phase octahedral tilt, $T''\rightarrow$tetragonal ($P4mm$) to cubic ($Pm\bar{3}m$) transition temperature.

depoling of NBT initiates at ~150 °C (T_2'), well below the depolarization temperature $T_d \sim 205$ °C, and is caused by abrupt decrease in the intrinsic polarization and antiphase octahedral tilt angle of the ferroelectric $R3c$ ferroelectric phase due to structural disorder caused by the onset of in-phase octahedral tilt. The system retains the memory of poling until 300 °C, i.e., the temperature (T_2) corresponding to the disappearance of the $R3c$ phase. The near overlap of T_d and T_2 in the composition range $0.03 \leqslant x \leqslant 0.05$ is correlated with the abrupt decrease in the difference between T_2 and T_2' (T_2-T_2' decreased sharply from 150 °C for $x = 0.00$ to ~10 °C for $x = 0.04$) due to significant reduction in the $R3c$-$P4bm$ transformation strain and associated kinetic barrier for this structural transformation. We also demonstrate that the appearance of the *ordered* $P4bm$ phase at room temperature in unpoled $0.03 \leqslant x \leqslant 0.05$ promotes conversion of Cc regions to $R3c$. For $x = 0.06$, we explain the crossover between T_2 and T_d (i.e., $T_d > T_2$) in terms of the sustenance of ferroelectricity beyond T_2 by the emergent $P4mm$ ferroelectric distortion. We have incorporated the findings presented here to draw updated phase diagrams of poled and unpoled NBT-BT.

ACKNOWLEDGMENTS

R.R. thanks the Science and Engineering Research Board (SERB) of the Department of Science and Technology, Govt. of India (Grant No. EMR/2016/001457), Naval Research Board (Grant No. NRB-467/MAT/20-21), and Space Technology Cell of IISc (Grant No. ISTC-443) for financial support.

[1] B. Jaffe, W. R. Cook, and H. Jaffe, *Piezoelectric Ceramics* (Academic Press, New York, 1971).
[2] European Commission, Directive 2011/65/EU of the European Parliament and of the Council of 8 June 2011 on the restriction of the use of certain hazardous substances in electrical and electronic equipment, Off. J. Eur. Union L **174**, 88 (2011).
[3] W. Liu and X. Ren, Phys. Rev. Lett. **103**, 257602 (2009).
[4] D. S. Keeble, F. Benabdallah, P. A. Thomas, M. Maglione, and J. Kreisel, Appl. Phys. Lett. **102**, 092903 (2013).
[5] D. Xue, Y. Zhou, H. Bao, J. Gao, C. Zhou, and X. Ren, Appl. Phys. Lett. **99**, 122901 (2011).
[6] D. Damjanovic, A. Biancoli, L. Batooli, A. Vahabzadeh, and J. Trodahl, Appl. Phys. Lett. **100**, 192907 (2012).
[7] M. Acosta, N. Khakpash, T. Someya, N. Novak, W. Jo, H. Nagata, G. A. Rossetti, Jr., and J. Rodel, Phys. Rev. B **91**, 104108 (2015).
[8] K. Brajesh, K. Tanwar, M. Abebe, and R. Ranjan, Phys. Rev. B **92**, 224112 (2015).
[9] K. Brajesh, M. Abebe, and R. Ranjan, Phys. Rev. B **94**, 104108 (2016).
[10] M. Abebe, K. Brajesh, A. Mishra, A. Senyshyn, and R. Ranjan, Phys. Rev. B **96**, 014113 (2017).
[11] A. Akbarzadeh, K. Brajesh, Y. Nahas, N. Kumar, S. Prokhorenko, D. Swain, S. Prosandeev, R. Walter, I. Kornev,J. Íñiguez, B. Dkhil, R. Ranjan, and L. Bellaiche, Phys. Rev. B **98**, 104101 (2018).

[12] Y. Nahas, A. R. Akbarzadeh, S. Prokhorenko, S. Prosandeev, R. Water, I. Kornev, J. Íñiguez, and L. Bellaiche, Nat. Commun. **8**, 15944 (2017).

[13] W. Ge, J. Li, D. Viehland, Y. Chang, and G. L. Messing, Phys. Rev. B **83**, 224110 (2011).

[14] Y. Dai, X. Zhang, and G. Zhou, Appl. Phys. Lett. **90**, 262903 (2007).

[15] Y. Saito, H. Takao, T. Tani, T. Nonoyama, K. Takatori, T. Homma, T. Nagaya, and M. Nakamura, Nature (London) **432**, 84 (2004).

[16] T. Iamsasri, G. Tutuncu, C. Uthaisar, S. Wongsaenmai, S. Pojprapai, and J. L. Jones, J. Appl. Phys. **117**, 024101 (2015).

[17] I. Levin, I. M. Reaney, E.-M. Anton,W. Jo, J. Rödel, J. Pokorny, L. A. Schmitt, H.-J. Kleebe, M. Hinterstein, and J. L. Jones, Phys. Rev. B **87**, 024113 (2013).

[18] G. D. Adhikary, B. Mahale, A. Senyshyn, and R. Ranjan, Phys. Rev. B **102**, 184113 (2020).

[19] R. Garg, B. N. Rao, A. Senyshyn, P. S. R. Krishna, and R. Ranjan, Phys. Rev. B **88**, 014103 (2013).

[20] R. Garg, B. N. Rao, A. Senyshyn, and R. Ranjan, J. Appl. Phys. **114**, 234102 (2013).

[21] G. D. Adhikary, D. K. Khatua, A. Senyshyn, and R. Ranjan, Acta Mater. **164**, 749 (2019).

[22] C. Ma, H. Guo, and X. Tan, Adv. Funct. Mater. **23**, 5261 (2013).

[23] B. N. Rao, D. K. Khatua, R. Garg, A. Senyshyn, and R. Ranjan, Phys. Rev. B **91**, 214116 (2015).

[24] G. D. Adhikary, D. K. Khatua, A. Senyshyn, and R. Ranjan, Phys. Rev. B **99**, 174112 (2019).

[25] K. Shibata, R. Wang, T. Tou, and J. Koruza, Mater. Res. Bull. **43**, 612 (2018).

[26] X. Liu and X. Tan, Adv. Mater. **28**, 574 (2016).

[27] S. T. Zhang, A. B. Kounga, E. Aulbach, H. Ehrenberg, and J. Rödel, Appl. Phys. Lett. **91**, 112906 (2007).

[28] A. K. Kalyani, K. Brajesh, A. Senyshyn, and R. Ranjan, Appl. Phys. Lett. **104**, 252906 (2014).

[29] A. R. Paterson, H. Nagata, X. Tan, J. E. Daniels, M. Hinterstein, R. Ranjan, P. B. Groszewicz, W. Jo, and J. L. Jones, MRS Bull. **43**, 600 (2018).

[30] I. G. Siny, C.-S. Tu, and V. H. Schmidt, Phys. Rev. B: Condens. Matter **51**, 5659 (1995).

[31] V. V. Shvartsman and D. C. Lupascu, J. Am. Ceram. Soc. **95**, 1 (2012).

[32] Y. Hiruma, H. Nagata, and T. Takenaka, J. Appl. Phys. **105**, 084112 (2009).

[33] G. O. Jones and P. A. Thomas, Acta Crystallogr. B **58**, 168 (2002).

[34] V. Dorcet and G. Trolliard, Acta Mater. **56**, 1753 (2008).

[35] A. M. Balagurov, E. Y. Koroleva, A. A. Naberezhnov, V. P. Sakhnenko, B. N. Savenko, N. V. Ter-Oganessian, and S. B. Vakhrushev, Phase Transitions **79**, 163 (2006).

[36] J. Kreisel, A. M. Glazer, P. Bouvier, and G. Lucazeau, Phys. Rev. B **63**, 174106 (2001).

[37] B. N. Rao, L. Olivi, V. Sathe, and R. Ranjan, Phys. Rev. B **93**, 024106 (2016).

[38] T.-M. Usher, I. Levin, J. E. Daniels, and J. L. Jones, Sci. Rep. **5**, 14678 (2015).

[39] E. Aksel, J. S. Forrester, J. L. Jones, P. A. Thomas, K. Page, and M. R. Suchomel, Appl. Phys. Lett. **98**, 152901 (2011).

[40] S. Gorfman and P. A. Thomas, J. Appl. Crystallogr. **43**, 1409 (2010).

[41] B. N. Rao, A. N. Fitch, and R. Ranjan, Phys. Rev. B **87**, 060102 (2013).

[42] G. A. Smolenskii, V. A. Isupov, A. I. Agranovskaya, and N. N. Krainik, Sov. Phys. Solid State **2**, 2982 (1960).

[43] B. N. Rao and R. Ranjan, Phys. Rev. B **86**, 134103 (2012).

[44] V. Dorcet, G. Trolliard, and P. Boullay, Chem. Mater. **20**, 5061 (2008).

[45] E. Aksel, J. S. Forrester, B. Kowalski, M. Deluca, D. Damjanovic, and J. L. Jones, Phys. Rev. B **85**, 024121 (2012).

[46] F. Cordero, F. Craciun, F. Trequattrini, E. Mercadelli, and C. Galassi, Phys. Rev. B **81**, 144124 (2010).

[47] E. Aksel, J. S. Forrester, B. Kowalski, J. L. Jones, and P. A. Thomas, Appl. Phys. Lett. **99**, 222901 (2011).

[48] B. N. Rao, R. Datta, S. S. Chandrashekaran, D. K. Mishra, V. Sathe, A. Senyshyn, and R. Ranjan, Phys. Rev. B **88**, 224103 (2013).

[49] B. Wylie-van Eerd, D. Damjanovic, N. Klein, N. Setter, and J. Trodahl, Phys. Rev. B **82**, 104112 (2010).

[50] K. Datta, R. B. Neder, A. Richter, M. Gobbels, J. C. Neuefeind, and B. Mihailova, Phys. Rev. B **97**, 184101 (2018).

[51] R. Ranjan, Curr. Sci. **118**, 1507 (2020).

[52] M. Otonicar, J. Park, M. Logar, G. Esteves, J. L. Jones, and B. Jancar, Acta Mater. **127**, 319 (2017).

[53] W. Jo, J. E. Daniels, J. L. Jones, X. Tan, P. A. Thomas, D. Damjanovic, and J. Rödel, J. Appl. Phys. **109**, 014110 (2011).

[54] B. N. Rao, M. Avdeev, B. Kennedy, and R. Ranjan, Phys. Rev. B **92**, 214107 (2015).

[55] J. E. Daniels, W. Jo, J. Rödel, and J. L. Jones, Appl. Phys. Lett. **95**, 032904 (2009).

[56] C. Ma, H. Guo, S. P. Beckman, and X. Tan, Phys. Rev. Lett. **109**, 107602 (2012).

[57] I. Levin and I. M. Reaney, Adv. Funct. Mater. **22**, 3445 (2012).

[58] W. Jo, J. Daniels, D. Damjanovic, W. Kleemann, and J. Rödel, Appl. Phys. Lett. **102**, 192903 (2013).

[59] W. Jo, S. Schaab, E. Sapper, L. A. Schmitt, H.-J. Kleebe, A. J. Bell, and J. Rödel, J. Appl. Phys. **110**, 074106 (2011).

[60] M. Hoelzel, A. Senyshyn, R. Gilles, H. Boysen, and H. Fuess, Neutron News **18**, 23 (2007).

[61] J. Rodrigues-Carvajal, *2000 FULLPROF. A Rietveld Refinement and Pattern Matching Analysis Program* (Laboratoire Leon Brillouin (CEACNRS), France).

[62] A. K. Kalyani, D. K. Khatua, B. Loukya, R. Datta, A. N. Fitch, A. Senyshyn, and R. Ranjan, Phys. Rev. B **91**, 104104 (2015).

[63] K. V. Lalitha, A. N. Fitch, and R. Ranjan, Phys. Rev. B **87**, 064106 (2013).

[64] A. K. Kalyani, H. Krishnan, A. Sen, A. Senyshyn, and R. Ranjan, Phys. Rev. B **91**, 024101 (2015).

[65] See Supplemental Material at http://link.aps.org/supplemental/10.1103/PhysRevB.103.184106 for information on (i) high-temperature NPD and XRPD patterns and Rietveld refinements of these patterns with appropriate structure models, and (ii) fitted structural parameters.

[66] H. D. Megaw and C. N. W. Darlington, Acta Crystallogr. Sect. A **31**, 161 (1975).

[67] A. M. Glazer and H. D. Megaw, Philos. Mag. **25**, 1119 (1972).

[68] G. D. Adhikary, D. K. Khatua, A. Mishra, A. De, N. Kumar, S. Saha, U. Shankar, A. Senyshyn, B. N. Rao, and R. Ranjan, Phys. Rev. B **100**, 134111 (2019).

[69] D. Viehland, S. J. Jang, L. E. Cross, and M. Wuttig, J. Appl. Phys. **68**, 2916 (1990).
[70] D. Viehland, M. Wuttig, and L. E. Cross, Ferroelectrics **120**, 71 (1991).
[71] V. Bobnar, Z. Kutnjak, R. Pirc, and A. Levstik, Phys. Rev. B: Condens. Matter **60**, 6420 (1999).
[72] R. Farhi, M. E. Marssi, J. L. Dellis, J. C. Picot, and A. Morell, Ferroelectrics **176**, 99 (1996).
[73] C. W. Ahn, C.-H. Hong, B.-Y. Choi, H.-P. Kim, H.-S. Han, Y. H. Hwang, W. Jo, K. Wang, J.-F. Li, J.-S. Lee, and I. W. Kim, J. Korean Phys. Soc. **68**, 1481 (2016).
[74] W. Jo, R. Dittmer, M. Acosta, J. Zang, C. Groh, E. Sapper, K. Wang, and J. Rödel, J. Electroceram. **29**, 71 (2012).
[75] L. E. Cross, Ferroelectrics **76**, 241 (1987).
[76] D. Fu, H. Taniguchi, M. Itoh, S. Koshihara, N. Yamamoto, and S. Mori, Phys. Rev. Lett. **103**, 207601 (2009).
[77] H. Wang, H. Xu, H. Luo, Z. Yin, A. A. Bokov, and Z.-G. Ye, Appl. Phys. Lett. **87**, 012904 (2005).
[78] D. Phelan, C. Stock, J. A. Rodriguez-Rivera, S. Chi, J. Leao, X. Long, Y. Xie, A. A. Bokov, Z.-G. Ye, P. Ganesh, and P. M. Gehring, Proc. Nat. Acad. Sci. USA **111**, 1754 (2014).
[79] S. Tinte, B. P. Burton, E. Cockayne, and U. V. Waghmare, Phys. Rev. Lett. **97**, 137601 (2006).
[80] T. Egami, Ferroelectrics **267**, 101 (2002).
[81] B. Dkhil, J. M. Kiat, G. Calvarin, G. Baldinozzi, S. B. Vakhrushev, and E. Suard, Phys. Rev. B **65**, 024104 (2001).
[82] V. Bobnar, Z. Kutnjak, R. Pirc, R. Blinc, and A. Levstik, Phys. Rev. Lett. **84**, 5892 (2000).
[83] D. Viehland, S. J. Jang, L. E. Cross, and M. Wuttig, J. Appl. Phys. **69**, 6595 (1991).
[84] Y. Hiruma, K. Yoshii, H. Nagata, and T. Takenaka, Ferroelectrics **346**, 114 (2007).